Comput Mech (2014) 54:71–83
DOI 10.1007/s00466-014-1031-3

ORIGINAL PAPER

Product properties of a two-phase magneto-electric composite: Synthesis and numerical modeling

Matthias Labusch · Morad Etier · Doru C. Lupascu · Jörg Schröder · Marc-André Keip

Received: 29 March 2014 / Accepted: 1 April 2014 / Published online: 1 May 2014

Abstract Magneto-electric (ME) materials are of high interest for a variety of advanced applications like in data storage and sensor technology. Due to the low ME coupling in natural materials, composite structures become relevant which generate the effective ME coupling as a strain-mediated product property. In this framework, it seems to be possible to achieve effective ME coefficients that can be exploited technologically. The present contribution investigates the realization of particulate ME composites with a focus on their experimental and computational characterization. We will show that different states of pre-polarizations of the ferroelectric material have a decisive influence on the overall obtainable ME coefficient. Details on the synthesis of two-phase composite microstructures consisting of a barium titanate matrix and cobalt ferrite inclusions will be discussed. Subsequently we will employ computational homogenization in order to determine the effective properties of the experimental composite numerically. We investigate the influence of different states of pre-polarization on the resulting ME-coefficients. For the numerical incorporation of the pre-polarization we use a heuristic method.

Keywords Modulus and composites · Homogenization · Materials processing · Product property · Magneto-electric composite

1 Introduction

In the last decades there has been a steady increase in attention to smart functional materials that couple different physical quantities to one another like, for example, polarization and strain or magnetization and strain. By using such materials smart applications in sensor and actuator technology can be realized. An important coupling phenomenon that attracts particular attention recently is the *magneto-electric* (ME) coupling property. Materials exhibiting pronounced couplings between magnetic and electric quantities could be used in a number of applications as, for example, in electrical magnetic-field sensors or electric-write magnetic-read memories, see e.g. [9]. The latter could be constructed as a so-called magneto-electric random access memory (MERAM), which would be realized by using materials that possess both *spontaneous magnetization and spontaneous polarization coupled to one another*, see, for example, [2]. A material that exhibits these two properties at the same time is termed *magneto-electric multiferroic*, where the term *multiferroic* defines a material that has at least two distinct ferroic states. Consequently, an

Contribution for the Special Issues on Modeling and Simulation of Advanced Manufacturing Processes-T. I. Zohdi, Handling Editor.

M. Labusch · J. Schröder (✉)
Institute of Mechanics, Department of Civil Engineering, Faculty of Engineering, University of Duisburg-Essen, Universitätsstraße 15, 45141 Essen, Germany
e-mail: j.schroeder@uni-due.de

M. Labusch
e-mail: matthias.labusch@uni-due.de

M. Etier · D. C. Lupascu
Institute for Materials Science and Center for Nanointegration Duisburg-Essen (CENIDE), University of Duisburg-Essen, Universitätsstraße 15, 45141 Essen, Germany
e-mail: morad.etier@uni-due.de

D. C. Lupascu
e-mail: doru.lupascu@uni-due.de

M.-A. Keip
Institute of Applied Mechanics (CE), Chair I, University of Stuttgart, Pfaffenwaldring 7, 70569 Stuttgart, Germany
e-mail: keip@mechbau.uni-stuttgart.de

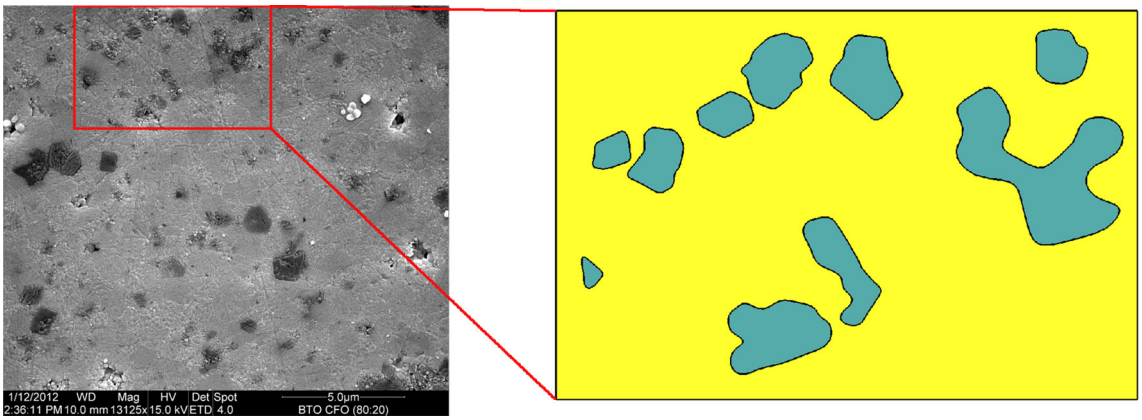

Fig. 1 Real composite microstructure with framed selected part

ME multiferroic is ferroelectric and ferromagnetic (which is often accompanied by a third ferroic state given by ferroelasticity). ME multiferroics have been investigated intensively, see for example [7,20,25,28,33,36,48,49]. However, since the ME coupling in natural materials is found to be very weak, see [6] who determined an upper bound for the possible ME coupling coefficient of single-phase materials, the development of *ME composite materials* consisting of electro-active and magneto-active phases becomes relevant. ME composites produce the desired ME coefficients as a *strain-mediated product property*, see, for example, [8,29,31,32,35,43,46]. A product property of a composite is defined as a property that is not present in each of its constituents, but appears effectively through their interaction; a general treatment on possible product properties is given in [44]. The ME coupling in a composite is generated through electrically or magnetically induced strain, where one distinguishes between the direct and the converse ME effect. The direct effect characterizes magnetically induced polarization: an applied magnetic field yields a deformation of the magneto-active phase that is transferred to the electro-active phase. As a result, this delivers *strain-induced polarization* in the electric phase. On the other hand, the converse effect characterizes electrically activated magnetization: an applied electric field yields a deformation of the electro-active phase which is transferred to the magneto-active material. This deformation then results in *strain-induced magnetization*. Several experiments on composite ME multiferroics showed remarkable ME coefficients that are orders of magnitudes higher than those of single-phase materials, see e.g. [14].

From a theoretical viewpoint the macroscopic characterization of ME composites – and therewith the *determination of their effective behavior* – is of particular interest. As a consequence, the development of suitable homogenization methods becomes important. In recent years, numerous analytical methods for the determination of the effective response of ME composites have been developed, see, for example, [3,4,17,18,22,30,42]. However, analytical schemes are often limited to specific microscopic morphologies, so that computational schemes are becoming relevant. One such method based on a finite-element (FE) discretization has been developed in [27] in order to determine the effective properties of piezomagnetic/piezoelectric ME composites.

In the present contribution we employ an extension of the work [39] to the case of magneto-electro-mechanical coupling, see [40] for details. We will focus on the *computational characterization of realistic, experimentally measured ME microstructures* and investigate implications that originate from specific assumptions of microscopic properties. The composite under consideration is depicted on the left hand side of Fig. 1. Here we see the morphology of a 0–3 particulate composite, where the brighter regions show the electro-active barium titanate ($BaTiO_3$) and the darker regions show the magneto-active cobalt ferrite ($CoFe_2O_4$). As implicitly defined above, we will denote the type of the composite by x–y with $\{x, y\} \in [1, 2, 3]$, where the first number indicates the spatial connectivity of the magneto-active phase and the second number indicates the connectivity of the electro-active phase.

In detail, the present paper reports on the investigation of experimental manufacturing and characterization techniques of ME composites as well as the associated implications for computational homogenization. Based on the homogenization procedure we compute the overall ME coefficient of two-phase composites consisting of piezoelectric and piezomagnetic phases. On the one hand, we apply the method to the simulation of idealized microstructures. Here, we compare our results to results taken from the literature [27] in order to validate the implemented model. On the other hand, we will apply the method to the computational characterization of a realistic microstructure, which we created using organosol crystallization. In this connection, we will discuss

the influence of constitutive assumptions made in the numerical model and its implications on the predictable effective ME coefficient. The outline of the paper is as follows. In Sect. 2 the theoretical framework will be provided where the procedure for the determination of the effective properties will be discussed in detail. Section 3 gives a brief overview on the experimental manufacturing of the composite sample and describes the used measuring technique. Afterwards in Sect. 4, several numerical examples with idealized and realistic two-phase composite microstructures will be performed. The effective properties of the real microstructure are then compared to experimental measurements. Different considerations of the polarization directions on the microscale demonstrate their influence on the effective ME coupling coefficient. Section 5 closes the paper with a short conclusion.

2 Theoretical framework

In the following the magneto–electro–mechanically coupled boundary value problem is briefly described. We set up the fundamental continuum balance equations and introduce the basic kinematic, electric and magnetic quantities. Furthermore, we outline the constitutive equations for the piezoelectric and piezomagnetic phase on the microscale. The main goal of this work is to characterize the constitutive behavior of ME composites at the macroscopic scale in consideration of the composition of the microstructure. Due to the leading part of the morphology of the microstructure with respect to the overall (macroscopic) ME coupling coefficient, we use a scale-transition between both scales, the macro- and the microscale. The scales are connected by a so-called localization and a homogenization step, where the latter one yields the effective properties of the composite, especially the overall ME-coefficient. In order to ease the readability of the following sections, we summarize the basic magneto–electro–mechanical quantities in Table 1.

Table 1 Magneto–electro–mechanical quantities and corresponding SI-Units

Symbol	Continuum mechanical description	SI-Unit
$\boldsymbol{u}$	Displacement vector	m
$\boldsymbol{\varepsilon}$	Linear strain tensor	1
$\boldsymbol{\sigma}$	Cauchy stress tensor	N/m^2
$\boldsymbol{t}$	Traction vector	N/m^2
$\boldsymbol{f}$	Mechanical body forces	N/m^3
ϕ_e	Electric potential	V
$\boldsymbol{E}$	Electric field vector	V/m
$\boldsymbol{D}$	Electric displacement vector	C/m^2
Q_e	Electric surface flux density	C/m^2
ρ	Density of free charge carriers	C/m^3
ϕ_m	Magnetic potential	A
$\boldsymbol{H}$	Magnetic field	A/m
$\boldsymbol{B}$	Magnetic flux density	Vs/m^2
Q_m	Magnetic surface flux density	Vs/m^2

2.1 Magneto–electro–mechanical boundary value problem

The considered micro-heterogeneous body $\mathcal{B} \subset \mathbb{R}^3$, characterized by a representative volume element $\mathcal{RVE} \subset \mathcal{B} \subset \mathbb{R}^3$ on the microscale, is parameterized with the coordinates $\boldsymbol{x}$. In order to capture the influence of the microstructure on the macroscopic behavior, we have to choose a suitable representative volume element which has to reflect the main mechanical, electrical, and magnetical characteristics of the microstructure. A periodic multiplication of the chosen $\mathcal{RVE}$ in all spatial directions is then imagined as an approximation of the real microstructure. The basic variables on the microscale, i.e., the linear strain tensor $\boldsymbol{\varepsilon}$, the electric field vector $\boldsymbol{E}$ and the magnetic field vector $\boldsymbol{H}$, are given by

$$\boldsymbol{\varepsilon} = \frac{1}{2}(\nabla \boldsymbol{u} + \nabla^T \boldsymbol{u}), \quad \boldsymbol{E} = -\nabla \phi_e \quad \text{and} \quad \boldsymbol{H} = -\nabla \phi_m. \tag{1}$$

The underlying fundamental balance equations are given by the balance of linear momentum, Gauß's law of electrostatics and Gauß's law of magnetostatics

$$\nabla \cdot \boldsymbol{\sigma} + \boldsymbol{f} = \boldsymbol{0}, \quad \nabla \cdot \boldsymbol{D} = \rho \quad \text{and} \quad \nabla \cdot \boldsymbol{B} = 0 \quad \text{in} \quad \mathcal{RVE}. \tag{2}$$

The associated macroscopic quantities are (under some technical assumptions) defined in terms of suitable volume averages. For simplicity, we restrict ourselves to the following definitions

$$\overline{\boldsymbol{\xi}} = \frac{1}{vol(\mathcal{RVE})} \int_{\mathcal{RVE}} \boldsymbol{\xi}\, dv \quad \text{with} \quad \{\boldsymbol{\xi} := \boldsymbol{\sigma}, \boldsymbol{\varepsilon}, \boldsymbol{D}, \boldsymbol{E}, \boldsymbol{B}, \boldsymbol{H}\}. \tag{3}$$

For a more general definition of the macroscopic quantities in terms of suitable surface integrals we refer to [37].

In order to derive energetically consistent boundary conditions in an algorithmically attractive representation we decompose the microscopic fields into the constant macroscopic part $\overline{\boldsymbol{\xi}}$ and a fluctuation part $\widetilde{\boldsymbol{\xi}}$, i.e.,

$$\boldsymbol{\xi} = \overline{\boldsymbol{\xi}} + \widetilde{\boldsymbol{\xi}} \quad \text{with} \quad \{\boldsymbol{\xi} := \boldsymbol{\sigma}, \boldsymbol{\varepsilon}, \boldsymbol{D}, \boldsymbol{E}, \boldsymbol{B}, \boldsymbol{H}\}. \tag{4}$$

For the construction of energetically consistent boundary conditions we postulate a generalized macrohomogeneity condition, which states the equality of the macroscopic and averaged microscopic power [21]

$$\overline{\boldsymbol{\sigma}} : \dot{\overline{\boldsymbol{\varepsilon}}} - \overline{\boldsymbol{D}} \cdot \dot{\overline{\boldsymbol{E}}} - \overline{\boldsymbol{B}} \cdot \dot{\overline{\boldsymbol{H}}} = \frac{1}{vol(\mathcal{RVE})} \int_{\mathcal{RVE}} (\boldsymbol{\sigma} : \dot{\boldsymbol{\varepsilon}} - \boldsymbol{D} \cdot \dot{\boldsymbol{E}} - \boldsymbol{B} \cdot \dot{\boldsymbol{H}})\, dv\,, \tag{5}$$

see also [37,39]. The macrohomogeneity condition is fulfilled by applying Dirichlet-, Neumann-, or periodic boundary conditions, for details see [40]. Furthermore, also the microscopic displacement field, the electric potential, and the magnetic potential are additively decomposed into affine and fluctuating parts

$$\boldsymbol{u} = \overline{\boldsymbol{\varepsilon}} \cdot \boldsymbol{x} + \widetilde{\boldsymbol{u}}, \quad \phi_e = -\overline{\boldsymbol{E}} \cdot \boldsymbol{x} + \widetilde{\phi}_e, \quad \phi_m = -\overline{\boldsymbol{H}} \cdot \boldsymbol{x} + \widetilde{\phi}_m, \tag{6}$$

respectively. Suitable periodic boundary conditions are

$$\begin{aligned} &\widetilde{\boldsymbol{u}}(\boldsymbol{x}^+) = \widetilde{\boldsymbol{u}}(\boldsymbol{x}^-) \quad \text{and} \quad \boldsymbol{t}(\boldsymbol{x}^+) = -\boldsymbol{t}(\boldsymbol{x}^-), \\ &\widetilde{\phi}_e(\boldsymbol{x}^+) = \widetilde{\phi}_e(\boldsymbol{x}^-) \quad \text{and} \quad Q_e(\boldsymbol{x}^+) = -Q_e(\boldsymbol{x}^-), \\ &\widetilde{\phi}_m(\boldsymbol{x}^+) = \widetilde{\phi}_m(\boldsymbol{x}^-) \quad \text{and} \quad Q_m(\boldsymbol{x}^+) = -Q_m(\boldsymbol{x}^-), \end{aligned} \tag{7}$$

where $\boldsymbol{x}^+$ and $\boldsymbol{x}^-$ denote associated points on the boundary of a periodic unit cell. After the solution of the boundary value problem, we can compute the homogenized macroscopic response by averaging over the microscopic fields over the $\mathcal{RVE}$.

2.2 Constitutive framework on the microscale

We analyze the magneto-electric coupling behavior of a two-phase composite containing a piezoelectric and a piezomagnetic phase. In our oversimplified model we assume a transversely isotropic linear material law for both phases on the microscale and make use of the constitutive framework proposed in [38], which can be analogously extended to magneto-electro-mechanically coupled problems. In detail, each phase is characterized by a preferred direction $\boldsymbol{a}$ in which the piezoelectric and piezomagnetic coupling is active, respectively. This preferred direction can be imagined as the direction of remanent polarization and magnetization, respectively. On the microscale the behavior of the two phases can be described by thermodynamical functions, which are defined for the piezoelectric phase as

$$\psi_e = \frac{1}{2}\boldsymbol{\varepsilon} : \mathbb{C}_e : \boldsymbol{\varepsilon} - \boldsymbol{E} \cdot \boldsymbol{e} : \boldsymbol{\varepsilon} - \frac{1}{2}\boldsymbol{E} \cdot \boldsymbol{\epsilon}_e \cdot \boldsymbol{E} - \frac{1}{2}\boldsymbol{H} \cdot \boldsymbol{\mu}_e \cdot \boldsymbol{H} \tag{8}$$

and for the piezomagnetic phase as

$$\psi_m = \frac{1}{2}\boldsymbol{\varepsilon} : \mathbb{C}_m : \boldsymbol{\varepsilon} - \boldsymbol{H} \cdot \boldsymbol{q} : \boldsymbol{\varepsilon} - \frac{1}{2}\boldsymbol{H} \cdot \boldsymbol{\mu}_m \cdot \boldsymbol{H} - \frac{1}{2}\boldsymbol{E} \cdot \boldsymbol{\epsilon}_m \cdot \boldsymbol{E}. \tag{9}$$

$\mathbb{C}$, $\boldsymbol{\epsilon}$, $\boldsymbol{\mu}$, $\boldsymbol{e}$ and $\boldsymbol{q}$ denote the tensors of elasticity, dielectric permittivity, magnetic permeability, piezoelectric coupling and piezomagnetic coupling of the individual electroactive and magnetoactive phases $\{e, m\}$, respectively. The function of the piezoelectric phase ψ_e includes a mechanical part, a coupling term between electric fields and mechanical strains as well as a purely electrical and a purely magnetical part. Analogously, the piezomagnetic energy ψ_m includes besides the mechanical part a coupling term between the mechanical strains and the magnetic field as well as a purely magnetical and a purely electrical part. For both phases we write down the incremental constitutive equations

$$\underbrace{\begin{bmatrix} \Delta\boldsymbol{\sigma}_{e,m} \\ -\Delta\boldsymbol{D}_{e,m} \\ -\Delta\boldsymbol{B}_{e,m} \end{bmatrix}}_{\mathfrak{S}} = \underbrace{\begin{bmatrix} \mathbb{C}_{e,m} & -\boldsymbol{e}_{e,m}^T & -\boldsymbol{q}_{e,m}^T \\ -\boldsymbol{e}_{e,m} & -\boldsymbol{\epsilon}_{e,m} & \boldsymbol{0} \\ -\boldsymbol{q}_{e,m} & \boldsymbol{0} & -\boldsymbol{\mu}_{e,m} \end{bmatrix}}_{\mathfrak{C}} \underbrace{\begin{bmatrix} \Delta\boldsymbol{\varepsilon}_{e,m} \\ \Delta\boldsymbol{E}_{e,m} \\ \Delta\boldsymbol{H}_{e,m} \end{bmatrix}}_{\mathfrak{D}}. \tag{10}$$

Here it has to be mentioned, that the ME coupling modulus for each of the two phases on the microscale, denoted by $\boldsymbol{\alpha}$, is equal to zero:

$$\boldsymbol{\alpha}_{e,m} \equiv \boldsymbol{0}. \tag{11}$$

However, the overall ME-coefficients are generally nonzero:

$$\overline{\boldsymbol{\alpha}} \neq \boldsymbol{0}. \tag{12}$$

One of the main goals of this contribution is to determine the effective ME coupling coefficient computationally and to compare the results with experimental observations.

2.3 Constitutive framework of ME composites on the macroscale

In order to approximate the ME coupling behavior on the macroscale, we assume the existence of an overall (macroscopic) thermodynamical function

$$\overline{\psi} = \frac{1}{2}\overline{\boldsymbol{\varepsilon}} : \overline{\mathbb{C}} : \overline{\boldsymbol{\varepsilon}} - \overline{\boldsymbol{H}} \cdot \overline{\boldsymbol{q}} : \overline{\boldsymbol{\varepsilon}} - \overline{\boldsymbol{E}} \cdot \overline{\boldsymbol{e}} : \overline{\boldsymbol{\varepsilon}} - \frac{1}{2}\overline{\boldsymbol{E}} \cdot \overline{\boldsymbol{\epsilon}} \cdot \overline{\boldsymbol{E}} - \frac{1}{2}\overline{\boldsymbol{H}} \cdot \overline{\boldsymbol{\mu}} \cdot \overline{\boldsymbol{H}} + \overline{\psi}_{ME}. \tag{13}$$

Obviously, the overall potential (13) reflects the characteristics of the functions (8) and (9) and has an *additional* essential contribution describing the ME-coupling. We define

$$\overline{\psi}_{ME} := -\overline{\boldsymbol{H}} \cdot \overline{\boldsymbol{\alpha}} \cdot \overline{\boldsymbol{E}}\,, \tag{14}$$

so that the effective ME coefficient appears as

$$\overline{\boldsymbol{\alpha}} = \frac{\partial \overline{\boldsymbol{B}}}{\partial \overline{\boldsymbol{E}}} = \left[\frac{\partial \overline{\boldsymbol{D}}}{\partial \overline{\boldsymbol{H}}}\right]^T \quad \text{with} \quad \overline{\boldsymbol{D}} = -\frac{\partial \overline{\psi}}{\partial \overline{\boldsymbol{E}}} \quad \text{and} \quad \overline{\boldsymbol{B}} = -\frac{\partial \overline{\psi}}{\partial \overline{\boldsymbol{H}}}. \tag{15}$$

Clearly, the ME coupling property of the composite arises as a product of the interaction between the individual phases. The interaction between the two phases is driven by the mechanical strains: on the one hand, an applied electric field induces a deformation of the electroactive material which is transferred to the magnetoactive material. The deformation of the magnetoactive material then induces a magnetic response. On the other hand, an applied magnetic field deforms the magnetic phase which then induces a strain-driven polarization in the electric phase. The remaining effective coefficients, the piezoelectric and piezomagnetic coupling moduli, are defined as

$$\overline{\boldsymbol{e}} = \frac{\partial \overline{\boldsymbol{D}}}{\partial \overline{\boldsymbol{\varepsilon}}} = -\left[\frac{\partial \overline{\boldsymbol{\sigma}}}{\partial \overline{\boldsymbol{E}}}\right]^T \quad \text{and} \quad \overline{\boldsymbol{q}} = \frac{\partial \overline{\boldsymbol{B}}}{\partial \overline{\boldsymbol{\varepsilon}}} = -\left[\frac{\partial \overline{\boldsymbol{\sigma}}}{\partial \overline{\boldsymbol{H}}}\right]^T \quad \text{with} \quad \overline{\boldsymbol{\sigma}} = \frac{\partial \overline{\psi}}{\partial \overline{\boldsymbol{\varepsilon}}}, \tag{16}$$

with $\{\overline{e}, \overline{q}\}^T_{ijk} = \{\overline{e}, \overline{q}\}_{kij}$. The effective elastic modulus, dielectric permittivity and magnetic permeability are determined by the derivatives

$$\overline{\mathbb{C}} = \frac{\partial \overline{\boldsymbol{\sigma}}}{\partial \overline{\boldsymbol{\varepsilon}}}, \qquad \overline{\boldsymbol{\epsilon}} = \frac{\partial \overline{\boldsymbol{D}}}{\partial \overline{\boldsymbol{E}}} \qquad \text{and} \qquad \overline{\boldsymbol{\mu}} = \frac{\partial \overline{\boldsymbol{B}}}{\partial \overline{\boldsymbol{H}}}. \tag{17}$$

In order to achieve a compact notation we write the macroscopic incremental constitutive equations in standard matrix form

$$\underbrace{\begin{bmatrix} \Delta\underline{\overline{\boldsymbol{\sigma}}} \\ -\Delta\underline{\overline{\boldsymbol{D}}} \\ -\Delta\underline{\overline{\boldsymbol{B}}} \end{bmatrix}}_{\underline{\overline{\mathfrak{S}}}} = \underbrace{\begin{bmatrix} \underline{\overline{\mathbb{C}}} & -\underline{\overline{\boldsymbol{e}}}^T & -\underline{\overline{\boldsymbol{q}}}^T \\ -\underline{\overline{\boldsymbol{e}}} & -\underline{\overline{\boldsymbol{\epsilon}}} & -\underline{\overline{\boldsymbol{\alpha}}}^T \\ -\underline{\overline{\boldsymbol{q}}} & -\underline{\overline{\boldsymbol{\alpha}}} & -\underline{\overline{\boldsymbol{\mu}}} \end{bmatrix}}_{\underline{\overline{\mathfrak{C}}}} \underbrace{\begin{bmatrix} \Delta\underline{\overline{\boldsymbol{\varepsilon}}} \\ \Delta\underline{\overline{\boldsymbol{E}}} \\ \Delta\underline{\overline{\boldsymbol{H}}} \end{bmatrix}}_{\underline{\overline{\mathfrak{D}}}}. \tag{18}$$

In order to solve (2) with the finite-element method, we formulate the associated weak forms of balance equations and approximate the displacements $\boldsymbol{u}$, the electric potential ϕ_e and the magnetic potential ϕ_m with suitable shape functions. We summarize the approximations of the basic field variables (1) on the microscale within a typical finite element as

$$\underline{\mathfrak{D}} = \underline{\mathbb{B}}\, \underline{\boldsymbol{d}}\,, \tag{19}$$

where the matrix $\underline{\mathbb{B}}$ contains the derivatives of the shape functions and the element vector $\underline{\boldsymbol{d}}$ contains the degrees of freedom, i.e. the displacements as well as the electric and magnetic potential. Following [40], we can compute the discrete values of the overall moduli $\underline{\overline{\mathfrak{C}}}$ on the fly during the iterative solution of the algebraic system of equations. The algorithmic expression for the overall moduli is

$$\underline{\overline{\mathfrak{C}}} = \langle \underline{\mathfrak{C}} \rangle - \frac{1}{vol(\mathcal{RVE})}\, \underline{\mathfrak{L}}^T\, \underline{\mathfrak{K}}^{-1}\, \underline{\mathfrak{L}}\,, \tag{20}$$

with the volume average of the moduli over the $\mathcal{RVE}$

$$\langle \underline{\mathfrak{C}} \rangle = \frac{1}{vol(\mathcal{RVE})} \int\limits_{\mathcal{RVE}} \underline{\mathfrak{C}}\, dv \tag{21}$$

and the FEM-matrices for the "generalized right-hand-sides" $\underline{\mathfrak{L}}$ and the global stiffness matrix for the unit-cell problem $\underline{\mathfrak{K}}$, i.e.,

$$\underline{\mathfrak{L}} = \int\limits_{\mathcal{RVE}} \underline{\mathbb{B}}^T\, \underline{\mathfrak{C}}\, dv \quad \text{and} \quad \underline{\mathfrak{K}} = \int\limits_{\mathcal{RVE}} \underline{\mathbb{B}}^T\, \underline{\mathfrak{C}}\, \underline{\mathbb{B}}\, dv. \tag{22}$$

3 Synthesis and manufacturing of ME composites

3.1 Synthesis schemes

The manufacturing approaches to magneto-electrics are highly depending on the nature of the resultant morphology [30]. Laminates (2–2 composites) can be easily manufactured by multiple methods depending on the dimensions of the intended composite. Thin films are grown by different methods well established in thin film technology like chemical vapor deposition (CVD), atomic layer deposition (ALD), sputtering, or laser ablation. Macroscopic laminates are generally glued together. Modeling of laminates is typically easy [18], because the boundary conditions are well set through the laminate structure for all fields, be they mechanical, electrical, or magnetic in nature. Laminates are presently the most effective structures for sensors if used on mechanically resonant very low stiffness beams [24]. 1D-composites like rod structures (1–3 structure) are harder to manufacture. First, rods have to be made and then appropriately aligned. Some direct growth techniques are available. Many subtractive techniques stem from the semiconductor industry. Lithography is the most widely used one. Typical feature sizes are in nanometer to micrometer range. Recently, additive manufacturing has become a broadly used tool in the larger micron to millimeter range. Here different pastes of materials are printed onto substrates layer by layer under computer control establishing an additive 3D structure, the simplest one being a rod structure. Subtractive techniques on the micron to millimeter range include dicing and etching. The latter may result in damage in sub-layers and structures. If the starting point for manufacturing is fibers, their alignment is a critical step in the process. One approach uses tape casting, where the flow dynamics of the highly viscous slurry under the doctor blade determines the orientation and degree of alignment of the fibers [34]. 0–3 structures require one component to

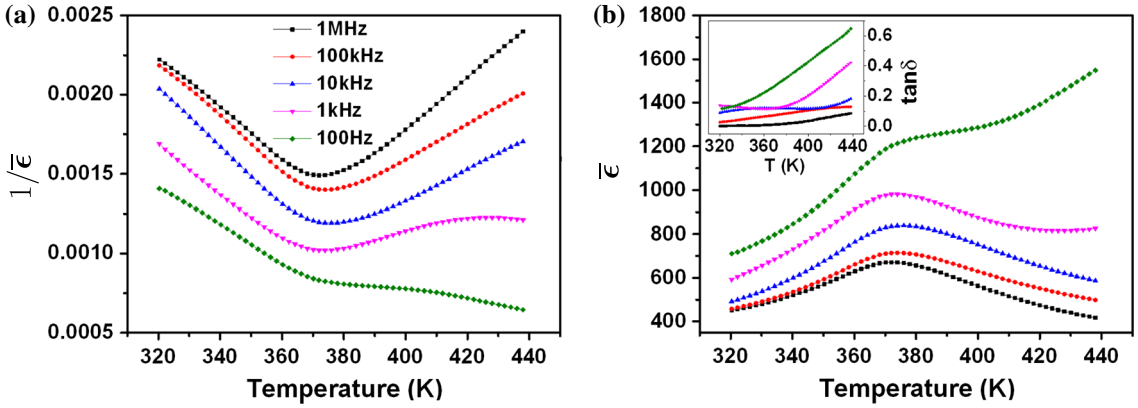

Fig. 2 Dielectric constant of 20/80 wt% $CoFe_2O_4$-$BaTiO_3$ (0–3) ceramic: **a** Curie–Weiss-Plot and **b** experimental raw data and losses

be completely embedded in another. This is typically appropriate, if two different powders are compacted, one dominating in volume content over the other, or if e.g. powders are embedded into polymers. Many different approaches have been taken. For the making of magneto-electric composites based on mechanical coupling, two issues are crucial: (i) good mechanical adhesion between both phases and (ii) good electrical resistivity, because otherwise the material will be short circuited electrically.

3.2 Synthesis results for 0–3 composites

One of the most fundamental issues in providing a suitable magneto-electric 0–3 composite experimentally is its macroscopic resistivity. If this value drops below a certain threshold, electric poling of the sample is no longer possible. In thin films, the growth techniques typically assure a dense microstructure also in the electrical sense proving to exhibit no percolating conductive component [1]. In ceramic processing, this kind of electrical microstructure can typically not be provided by classical synthesis techniques like solid state reaction [16]. We recently developed the organosol route [15]. This method was adopted to coat the $CoFe_2O_4$ nanoparticles already in suspension. Subsequent densification during sintering then proved to be sufficiently gentle with this structure to generate a micron sized microstructure of non percolating $CoFe_2O_4$ particles in the system. In order to assure a robust system, we chose 20/80 for the present study containing a much higher content of the insulating ferroelectric than the partly conductive magnetostrictive component. This yielded a very suitable resistivity of the material of $\rho = 60\ G\Omega\ cm$ which permitted poling of the sample. The relative difference in elastic modulus is small and thus equal volume contents of both constituents should provide best coupling coefficient.

Experimentally, it is clear that $BaTiO_3$ slightly changes its character in the composite. While in the single crystal and in mono-phase bulk ceramics, $BaTiO_3$ exhibits a clear first order phase transition. This typically entails a peak in dielectric constant and a step in its inverse [23]. While in our samples the Curie temperature is unchanged with respect to the pure phase ceramics, a broader distribution of the peak value is found (Fig. 2). Also the Curie–Weiss-Plot for $BaTiO_3$ should exhibit a fairly sharp minimum in $1/\epsilon$ which is broadened here. This is typical in nanograin materials [45], while micron size pure $BaTiO_3$ displays sharp maxima in ϵ even though there is a strong dependence of the explicit values of the dielectric constant at the phase transition points [26]. Thus, the grain size of our $BaTiO_3$-component in the magneto-electric composite ceramic does exhibit the expected behavior for its grain size. No unexpected modification of the ferroelectric phase is observed. We also found no anomaly of the dielectric constant as reported in [19] which is likely an effect of high conductivity above the Curie point suggesting acceptor doping of $BaTiO_3$ in their samples [47]. Actually, our route obviously never showed any occurrence of such doping in the $BaTiO_3$-phase and the concurrent increase in conductivity of the ferroelectric part of the composite in our route. The somewhat increasing conductivity (apparent increase in $\bar{\epsilon}$) at low frequency and high temperature indicates a classical thermally activated transport process at medium distances, thus percolating conductive grains, but sufficiently small in cluster size not to short-circuit the entire sample.

3.3 Experimental details

The $CoFe_2O_4/BaTiO_3$ nanoparticles with core/shell structure were synthesized via organosol crystallization, see [10,12]. Initially, co-precipitation was used to synthesize $CoFe_2O_4$ particles with a mean size < 40 nm as described in detail in [12]. A stable ferrofluid of $CoFe_2O_4$ nanopowder was added to a tetramethyl-ammonium hydroxide (TMAH) solution containing the amorphous barium titanate precursor. The relative ratio of weights in the final products was adjusted by the amounts of the cobalt ferrite powder and

barium titanate in the precursors yielding 20/80 by weight $CoFe_2O_4/BaTiO_3$. In order to achieve high electrical resistivity of the overall sample and optimal coupling in between the two phases, the cobalt iron oxide particles must be well distributed in the microstructure. This was assured by rotation milling for about 12 h. The powder was then washed several times with ethanol, dried at room temperature under a fume hood, and ultimately calcinated at 750°C for 15 minutes. Disks were pressed with a hydraulic press into disk-shaped pellets with diameter of 8 mm and thickness of 0.6 mm under 5 tons load. The discs were sintered into ceramics at 1, 200°C for 2 h. For comparison, pure cobalt ferrite and barium titanate ceramic samples were sintered alike. X-ray diffraction determined the phase content of the composites (Siemens D-5000 with Cu-Kα radiation at steps of $\delta(2\Theta) = 0.01°$ with a time constant of 1 s). Scanning and transmission electron microscopy (SEM and TEM) confirmed the morphology and structure of the specimens (SEM quanta 400 FEG and TEM TECNAI F20). Before SEM measurements, the ceramic samples were well polished and chemically etched. The particle/grain size distribution was analyzed by the analySIS software (Soft Imaging Systems). A self-built Sawyer-Tower circuit at a frequency of 250 Hz served to determine the electric field dependence of polarization. For electrical measurements silver electrodes were fired onto both sides of the samples at 500°C. The magnetic properties as determined by SQUID magnetometry in the temperature interval from 5 to 300 K at magnetic fields up to 1 T can be found in [13]. Magneto-electric measurements were performed using a modified SQUID ac susceptometer in the temperature range 200–300 K at electric fields up to 1 kV/cm and a magnetic field of 0.15 T. The method is described in principles in [5]. In general, an ac electric field, $E = E_{ac}\cos(\omega t)$ generates an induced magnetic signal. The first harmonic of this magneto-electrically induced ac magnetic moment, $m' = m_{ME}\cos(\omega t)$, is detected using an internal lock-in amplifier. The converse magneto-electric coefficient, α_C, can be estimated from the ac electric field dependence of the induced magnetization, $\alpha_C = M_{ME}\mu_0/E_{ac}$, where $M_{ME} = m_{ME}/V_s$ is the magneto-electrically induced magnetization, V_s is the sample volume, and μ_0 is the permeability of free space. The advantage of this method is its high sensitivity. The smallest measurable ME coefficient ranges around 0.01×10^{-12} s/m.

4 Computational determination of magneto-electro-mechanical properties of ME composites

For the simulation of magneto-electric composites we consider different types of microstructures. First, in order to validate the implemented model, we consider a boundary value problem from the work [27]. After that, we compute the effective material behavior of an experimental ME microstructure consisting of a piezoelectric $BaTiO_3$ matrix and piezomagnetic $CoFe_2O_4$ inclusions discussed in the previous paragraphs. The computationally determined ME coefficients are then compared to the experimentally measured data. In all calculations we consider periodic boundary conditions on the microscale.

Table 2 Material parameters

Parameter	Unit	$BaTiO_3$	$CoFe_2O_4$
$\mathbb{C}_{11}$	N/mm^2	16.6×10^4	28.60×10^4
$\mathbb{C}_{12}$	N/mm^2	7.7×10^4	17.30×10^4
$\mathbb{C}_{13}$	N/mm^2	7.8×10^4	17.05×10^4
$\mathbb{C}_{33}$	N/mm^2	16.2×10^4	26.95×10^4
$\mathbb{C}_{44}$	N/mm^2	4.3×10^4	4.53×10^4
ϵ_{11}	mC/kVm	112×10^{-4}	0.80×10^{-4}
ϵ_{33}	mC/kVm	126×10^{-4}	0.93×10^{-4}
μ_{11}	N/kA^2	5.0	157.0
μ_{33}	N/kA^2	10.0	157.0
e_{31}	C/m^2	−4.4	0.0
e_{33}	C/m^2	18.6	0.0
e_{15}	C/m^2	11.6	0.0
q_{31}	N/kAmm	0.0	580.3
q_{33}	N/kAmm	0.0	−699.7
q_{15}	N/kAmm	0.0	550.0

The material parameters of the two phases are adopted from the work [27] and are listed in Table 2. They, however, differ for cobalt ferrite from the parameters used in the reference publication in such a way that we set $\mu_{11} := 157\,\text{N/kA}^2$, see also [41]. Second, the piezomagnetic coefficient q_{33} is set to $q_{33} := -699.7\,\text{N/kAmm}$, c.f. [3][1].

4.1 Computational characterization of the magneto-electro-mechanical properties of an ideal microstructure

In order to validate the implemented material model we perform simulations of an ideal three-dimensional $\mathcal{RVE}$ taken from [27]. The $\mathcal{RVE}$ consists of a cubic piezomagnetic $CoFe_2O_4$ matrix and a cylindrical piezoelectric $BaTiO_3$ inclusion oriented in vertical direction. In analogy to the reference publication, the preferred directions of the two phases are assumed to point in positive vertical direction. For the description of both materials we use the set of material parameters given in [27]. This means that in this computation we set $\mu_{11} := -590\,\text{N/kA}^2$ and $q_{33} := +699.7\,\text{N/kAmm}$.

[1] In the work [27] these parameters are given by $\mu_{11} = -590\,\text{N/kA}^2$ and $q_{33} = +699.7\,\text{N/kAmm}$.

We perform calculations with five different $\mathcal{RVE}$s characterized by volume fractions of 30, 40, 50, 60 and 70 % of the inclusion. For an illustration of the $\mathcal{RVE}$ with 40 % volume fraction of the inclusion see Fig. 3a.

We apply a macroscopic electric field $\overline{\boldsymbol{E}} := [0, 0, \overline{E}_3]^T$. This field is transferred to the microscopic $\mathcal{RVE}$ using periodic boundary conditions. Due to the preferred orientation of the piezoelectric phase and the applied field, the inclusion reacts with an elongation in vertical direction. This deformation is transferred to the piezomagnetic phase, which leads to magnetization of the matrix. This strain-mediated coupling gives rise to a magneto-electric coupling coefficient that can be determined formally by

$$\overline{\boldsymbol{\alpha}} = \frac{\partial \overline{\boldsymbol{B}}}{\partial \overline{\boldsymbol{E}}} = \left[\frac{\partial \overline{\boldsymbol{D}}}{\partial \overline{\boldsymbol{H}}}\right]^T, \tag{23}$$

which is evaluated using (20). The resulting ME coefficients are calculated for the different volume fractions of $BaTiO_3$ and are in perfect agreement with the results from [27], see Fig. 3b. For completeness, the following graphs show the computed effective elastic, dielectric, magnetic, piezoelectric, piezomagnetic and ME coefficients of the composite. (Figs. 4, 5, 6).

4.2 Computational characterization of the magneto-electro-mechanical properties of a real microstructure

Now we apply the computational method to the determination of the ME properties of the real composite microstructure discussed in Sect. 3. In Fig. 7 an electron microscopy image of the composite is shown, where the different phases are visible due to the slightly distinct local conductivity. The brighter areas reflect the piezoelectric barium titanate and the darker areas show the piezomagnetic cobalt ferrite.

The mass fractions of barium titanate and cobalt ferrite are 80 and 20 %, respectively. Taking into account the densities of the two phases we use a sample with 16.5 % surface fraction

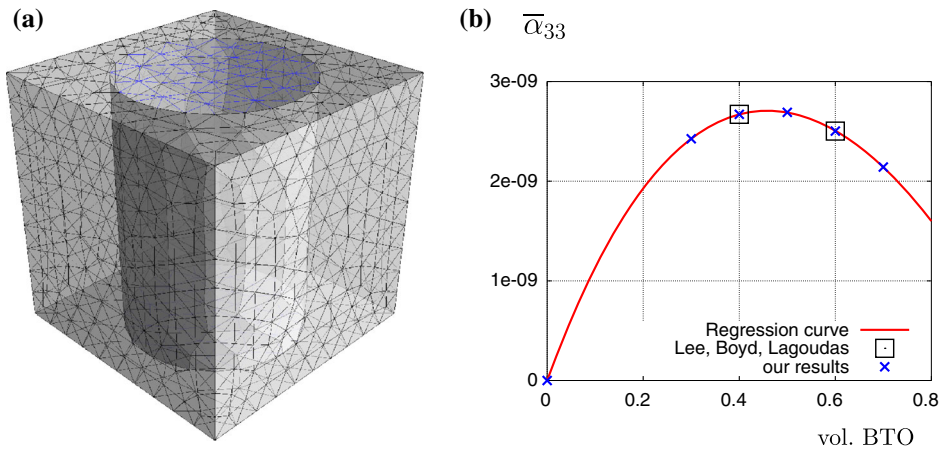

Fig. 3 **a** $\mathcal{RVE}$ consisting of a piezomagnetic cube with a piezoelectric cylindrical inclusion and **b** comparison of the determined ME-coefficient with results from [27]; please note, that the magnetic permeability is set to $\mu_{11} = -590\,\mathrm{N/kA^2}$ and the piezomagnetic coefficient q_{33} is set to $q_{33} = +699.7\,\mathrm{N/kAmm}$

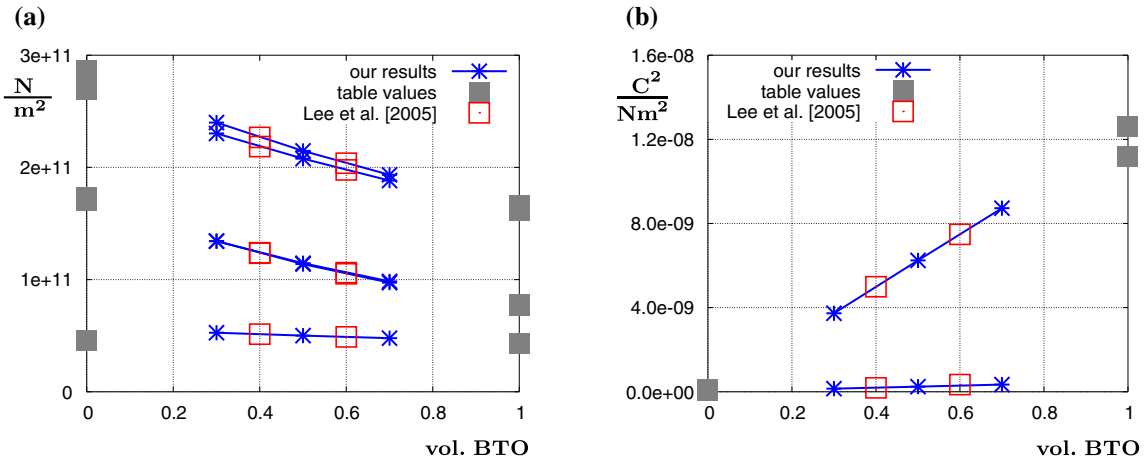

Fig. 4 Effective properties of **a** elastic moduli, **b** dielectric permittivity depending on vol. BTO

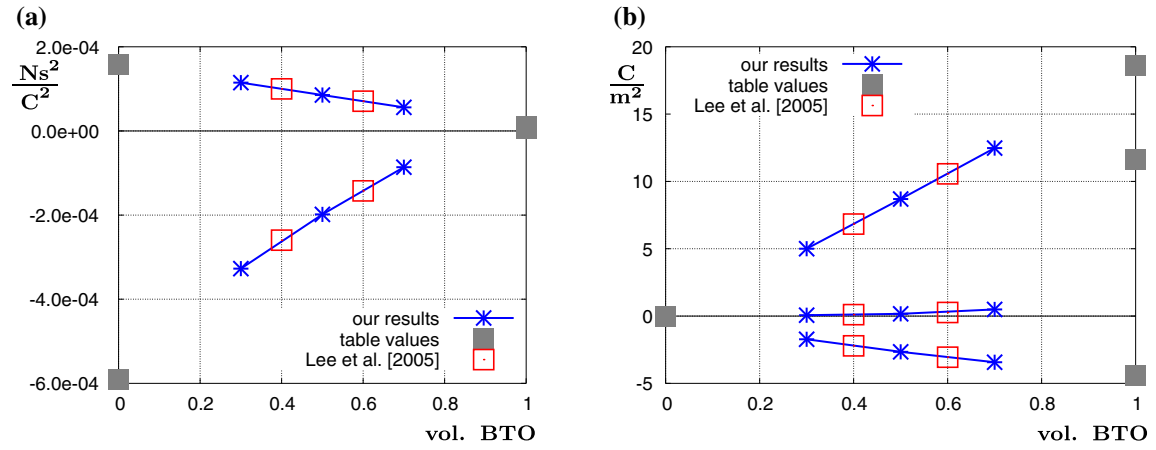

Fig. 5 Effective properties of **a** magnetic permeability, **b** piezoelectric constants depending on vol. BTO

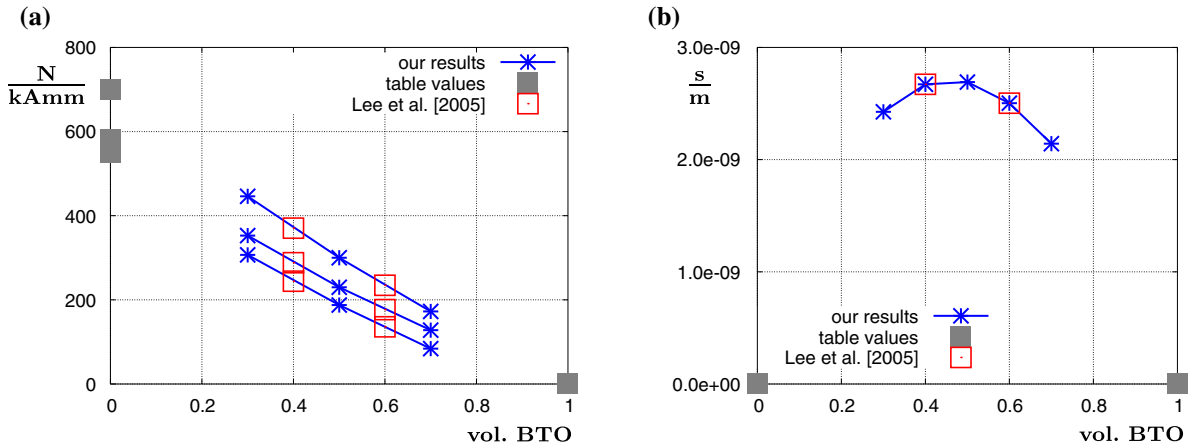

Fig. 6 Effective properties of **a** piezomagnetic constants, **b** ME-coefficient depending on vol. BTO

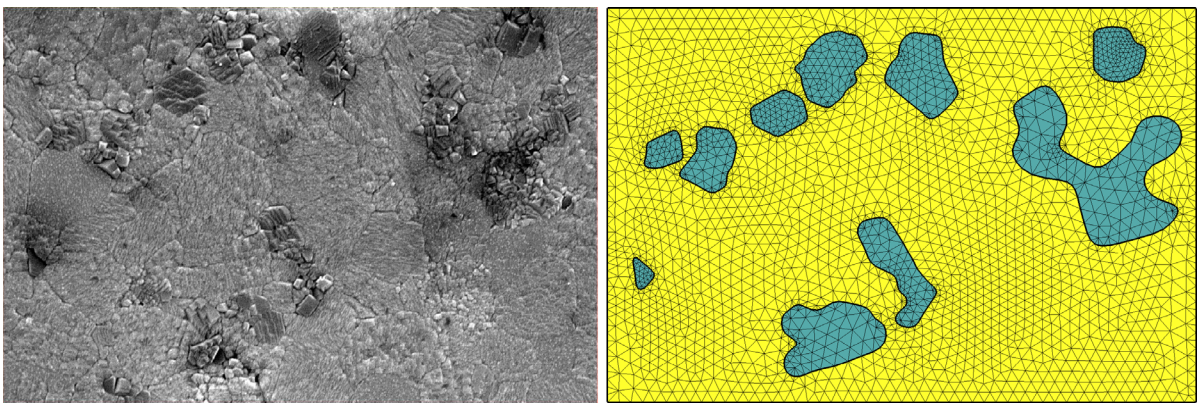

Fig. 7 Electron microscopy image of the composite microstructure (*left*) and finite element discretization (*right*), see also Fig. 1

of the inclusion. The two-dimensional microstructure is then discretized with 5,324 quadratic triangular finite elements.

In a particulate ME composite the quality of ME coupling strongly depends on the pre-polarization and pre-magnetization of the individual phases. In order to analyze the effect of ferroelectric pre-polarization we will take into account different scenarios for the remanent pre-polarization. We incorporate the pre-polarization in the following way. As a first step, we apply a macroscopic electric field in vertical direction on the initially unpolarized microstructure. That means we set $\overline{\boldsymbol{E}} = [0, \overline{E}_2, 0]^T, \overline{\boldsymbol{\varepsilon}} = \boldsymbol{0}$ and $\overline{\boldsymbol{H}} = \boldsymbol{0}$ in (6). In this first step the piezoelectric coupling parameters on the

Table 3 Determination of piezoelectric coupling properties on the microscale

1. Set initial preferred direction $\boldsymbol{a}_0 = [0, 1, 0]$
2. Neglect constitutive couplings: set piezoelectric moduli equal zero $\boldsymbol{e} \equiv \boldsymbol{0}$
3. Apply macroscopic electric field $\overline{\boldsymbol{E}} = c_1^+ \boldsymbol{a}$; compute local distribution of $\boldsymbol{E}$
4. Choose preferred directions $\boldsymbol{a}$ (for each Gauss point): $\boldsymbol{a} = \boldsymbol{E}/\|\boldsymbol{E}\|$
5. Estimate relative amplitude of remanent polarization $p_s = \tanh(c \cdot ||\boldsymbol{E}||) \in [0, 1)$
6. Determine piezoelectric moduli $\boldsymbol{e} = p_s(-\beta_1 \boldsymbol{a} \otimes \boldsymbol{1} - \beta_2 \boldsymbol{a} \otimes \boldsymbol{a} \otimes \boldsymbol{a} - \beta_3 \hat{\boldsymbol{e}})$ with $\{\hat{e}\}_{kij} := \frac{1}{2}[a_i \delta_{kj} + a_j \delta_{ki}]$

microstructure are set to zero. As a result of the macroscopic loading and the inhomogeneous distribution of the composite properties an inhomogeneous distribution of the electric field on the microscale is obtained. We use these electric field vectors to define the pre-polarization state of the piezoelectric matrix: first, the direction of the microscopic electric field is used to define the preferred direction $\boldsymbol{a}$ of the transversely isotropic model, i.e. we set $\boldsymbol{a} := \boldsymbol{E}/\|\boldsymbol{E}\|$ in each integration point on the microscale. Second, the norm of the electric field is used to define the amount of piezoelectric coupling at each particular integration point. The scaling is described by a factor p_s defined by a hyperbolic tangent function

$$p_s = \tanh(c \cdot ||\boldsymbol{E}||). \tag{24}$$

where the factor c defines the slope of the hyperbolic tangent. In the next examples the value of c is set to 2 mm/kV in order to approximate the polarization behavior of barium titanate. By using this scaling factor, areas with high electric fields are characterized by higher piezoelectric coupling. For convenience, the algorithmic treatment is summarized in Table 3.

In the following simulations we will apply different macroscopic electric fields in the range between 0.01 and 3kV/mm, which will lead to different pre-polarization states on the microstructure. We will then analyze the influence of the pre-polarization states on the overall ME coupling. The pre-magnetization directions of the piezomagnetic inclusions are assumed to point perfectly in vertical direction with fully activated coupling parameters.

Figure 8 shows the pre-polarization directions as well as the distribution of the amount of pre-polarization for two different applied macroscopic electric fields of magnitude $\overline{E}_2 = 0.5\,\mathrm{kV/mm}$ and $\overline{E}_2 = 1\,\mathrm{kV/mm}$.

As can be seen the electric field in the matrix concentrates between the inclusions with maximum values in the areas with high surface fraction of the inclusion material. This is due to the lower dielectric permittivity of the inclusions. In these concentrated areas the electric fields are associated to a saturation of the hyperbolic function in (24). Thus, full pre-polarization of the matrix material is obtained.

Now having incorporated the pre-polarization of the ferroelectric matrix we can analyze the magneto-electro-mechanical behavior of the composite. In order to do so we load the pre-polarized specimen again with an electric field and study the resulting magneto-electric interactions on the microscale. In the following Fig, 9a we see the distributions of microscopic electric potential and electric field that arise as a consequence of an applied macroscopic electric field of $\overline{E}_2 = 1\,\mathrm{kV/mm}$. Due to the piezoelectric coupling of the matrix this electric field yields a deformation that is mediated to the inclusions. Since we assumed piezomagnetic coupling in the inclusions we arrive at a magnetic reaction. In Fig. 9b the strain-induced distribution of the magnetic potential as well as the vectors of magnetic flux density are shown.

As mentioned earlier, we applied different macroscopic electric pre-polarization fields in order to arrive at different

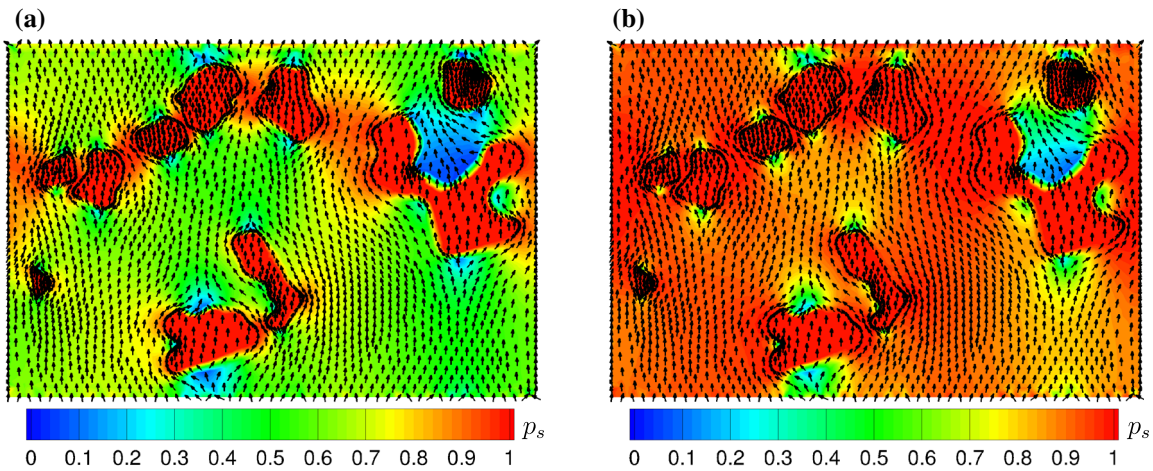

Fig. 8 Distribution of p_s (*contour*) with preferred directions $\boldsymbol{a}$ (*vectors*) for applied electric fields $\overline{E}_2 = 0.5\,\mathrm{kV/mm}$ (**a**) and $\overline{E}_2 = 1\,\mathrm{kV/mm}$ (**b**)

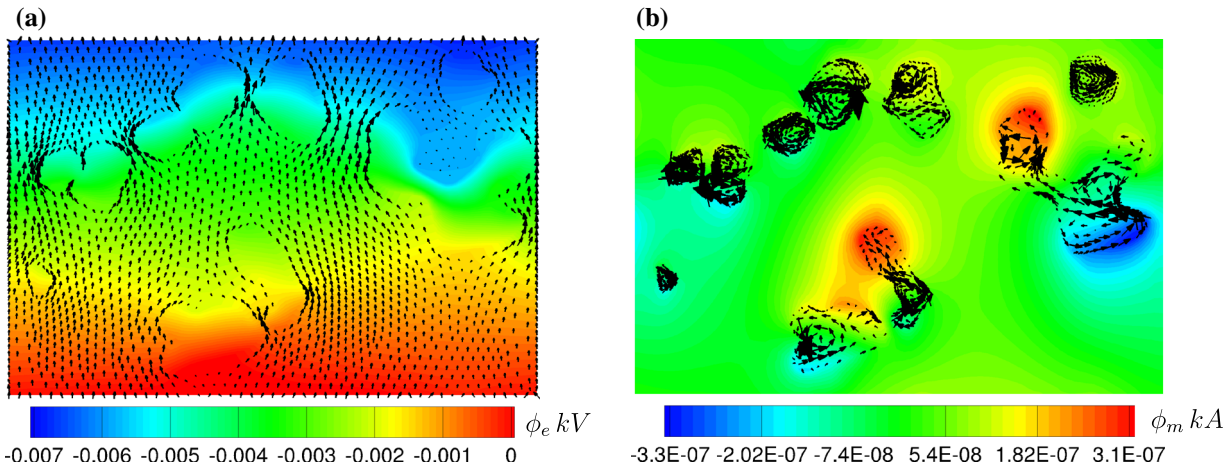

Fig. 9 **a** Electric potential ϕ_e with electric field vectors $\boldsymbol{E}$ in the piezoelectric matrix and **b** magnetic potential ϕ_m with magnetic flux density vectors $\boldsymbol{B}$ in the inclusions for $\overline{E}_2 = 1\,\mathrm{kV/mm}$

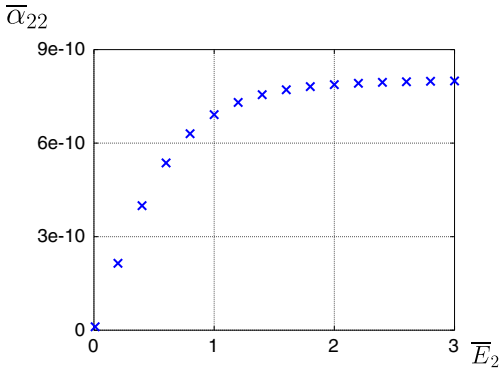

Fig. 10 Magneto-electric coupling coefficient $\overline{\alpha}_{22}$ in s/m for different electric fields $\overline{E}_2$ in kV/mm

states of pre-polarization on the microlevel. As can be seen in Fig. 10 the intensity of the pre-polarization field has a strong influence on the overall ME coupling.

For high pre-polarization fields the ME-coefficient saturates to the value of $\overline{\alpha}_{22} \approx 8.04 \times 10^{-10}\,\mathrm{s/m}$. For comparison, [11] measured an effective ME-coefficient of $\overline{\alpha}_{22} \approx 4.4 \times 10^{-12}\,\mathrm{s/m}$ of the sample. This rather large deviation allows for mainly two possible conclusions. On the one hand, on the modeling side, the method for the incorporation of ferroelectric pre-polarization was very simplified in nature and will be enhanced in future developments. Furthermore, the assumption of perfect pre-magnetization in the inclusions was very optimistic. In addition to that, the two-dimensional approximation of the particulate microstructure introduces another source for deviations. On the other hand, the simulations clearly indicate that there is still the need for improvement for the experimental preparation since an optimal pre-polarization and/or pre-magnetization state has not been obtained. In any case there will also be additional properties on the microscale that we have to address in future developments. One such property is the experimentally very relevant electric conductivity. Thus, the challenge for the experimental side now resides in assuring high resistivity in compositions of higher contents in the piezomagnetic phase which by nature of the coupling through strain should yield maximized coefficients near volume ratios of 50/50.

5 Conclusion

The paper discussed aspects of experimental manufacturing of multiferroic composites and a numerical formulation for the characterization of such composites. Due to the fact that the effective macroscopic magneto-electric coupling significantly depends on the composition and morphology of the microstructure, we used a computational homogenization procedure based on the FE^2 method which can be applied to arbitrary microstructural morphologies. This method was applied to two different kinds of microstructures. On the one hand, idealized microstructures taken from the literature were used to validate the implemented model. On the other hand, the method was applied to the characterization of a realistic microstructure, which was manufactured and measured in experiments. Due to the fact that the magneto-electric coupling in a real sample has to be activated through pre-polarization of the electroactive phase, we considered different pre-polarization states of the piezoelectric matrix. The comparison between the experimental and computational results showed a rather large deviation. This could be explained by the partly oversimplified modeling assumptions and the experimentally not yet obtained optimal pre-polarization and -magnetization state.

Acknowledgments We gratefully acknowledge the financial support by the "Deutsche Forschungsgemeinschaft" (DFG), research group "Ferroische Funktionsmaterialien - Mehrskalige Modellierung

und experimentelle Charakterisierung", project 1 (SCHR 570/12-1) and project 2 (LU 729/12). Morad Etier acknowledges support by the DAAD-GRISEC program (Grant 50750877). Furthermore, we acknowledge the comprehensive discussions and suggestions by Dr. Vladimir V. Shvartsman.

References

1. Bai F, Zhang H, Li J, Viehland D (2010) Magnetic and magnetoelectric properties of as deposited and annealed batio3-cofe2o4 nanocomposite thin films. J Phys D 43:509901
2. Bibes M, Barthélémy A (2008) Multiferroics: towards a magnetoelectric memory. Nat Mater 7(6):425–426
3. Bichurin M, Petrov V, Srinivasan G (2003) Theory of low-frequency magnetoelectric coupling in magnetostrictive-piezoelectric bilayers. Phys Rev B 68(5):054,402
4. Bichurin M, Petrov V, Averkin S, Liverts E (2010) Present status of theoretical modeling the magnetoelectric effect in magnetostrictive-piezoelectric nanostructures. Part I: Low frequency and electromechanical resonance ranges. J Appl Phys 107(5):053,904
5. Borisov P, Hochstrat A, Shvartsman V, Kleemann W (2007) Superconducting quantum interference device setup for magnetoelectric measurements. Rev Sci Instrum 78:106105–106108
6. Brown WF, Hornreich R, Shtrikman S (1968) Upper bound on the magnetoelectric susceptibility. Phys Rev 168(2):574–577
7. Cheong SW, Mostovoy M (2007) Multiferroics: a magnetic twist for ferroelectricity. Nat Mater 6(1):13–20
8. Eerenstein W, Mathur ND, Scott JF (2006) Multiferroic and magnetoelectric materials. Nature 442(7104):759–765
9. Eerenstein W, Wiora M, Prieto J, Scott JF, Mathur N (2007) Giant sharp and persistent converse magnetoelectric effects in multiferroic epitaxial heterostructures. Nat Mater 6(5):348–351
10. Etier M, Gao Y, Shvartsman V, Elsukova A, Landers J, Wende H, Lupascu D (2012a) Cobalt ferrite/barium titanate core/shell nanoparticles. Ferroelectrics 438:115–122
11. Etier M, Gao Y, Shvartsman VV, Lupascu DC, Landers J, Wende H (2012b) Magnetoelectric properties of $0.2cofe_2o_4$-$0.8batio_3$ composite prepared by organic method. In: Proceedings of the European conference on the applications of polar dielectrics pp 1–4
12. Etier M, Shvartsman V, Stromberg F, Landers J, Wende H, Lupascu D (2012c), Synthesis and magnetic properties of cobalt ferrite nanoparticles. In: Materials Research Society symposium proceedings, vol 1398
13. Etier M, Shvartsman V, Gao Y, Landers J, Wende H, Lupascu D (2013) Magnetoelectric effect in (0–3) CoFe2O4-BaTiO3 (20/80) composite ceramics prepared by the organosol route. Ferroelectrics 448:77–85
14. Fiebig M (2005) Revival of the magnetoelectric effect. J Phys D 38(8):R123–R152
15. Gao Y, Shvartsman V, Elsukova A, Lupascu D (2012) Low-temperature synthesis of crystalline batio3 nanoparticlesby one-step "organosol"-precipitation. J Mater Chem 22:17573–17583
16. Hanumaiah A, Bhimasankaram T, Suryanarayana S, Kumar G (1994) Dielectric behavior and magnetoelectric effect in cobalt ferrite-barium titanate composites. Bull Mater Sci 17:405–409
17. Harshé G, Dougherty J, Newnham RE (1993a) Theoretical modeling of 3–0/0–3 magnetoelectric composites. Int J Appl Electromagn Mater 4:161–171
18. Harshé G, Dougherty J, Newnham RE (1993b) Theoretical modeling of multilayer magnetoelectric composites. Int J Appl Electromagn Mater 4:145–159
19. Hemeda O, Tawfik A, Amer M, Kamal B, Refaay DE (2012) Structural, spectral and dielectric properties of piezoelectric-piezomagnetic composites. J Magn Magn Mater 324:3229–3237
20. Hill N (2000) Why are there so few magnetic ferroelectrics? J Phys Chem B 104:6694–6709
21. Hill R (1963) Elastic properties of reinforced solids—some theoretical principles. J Mech Phys Solids 11:357–372
22. Huang JH, Kuo WS (1997) The analysis of piezoelectric/piezomagnetic composite materials containing ellipsoidal inclusions. J Appl Phys 81(3):1378–1386
23. Jaffe B, Cook WR Jr, Jaffe H (1971) Piezoelectric ceramics. Academic Press, London
24. Jahns R, Piorra A, Lage E, Kirchhof C, Meyners D, Gugat J, Krantz M, Gerken M, Knöchel R, Quandt E (2013) Giant magnetoelectric effect in thin-film composites. J Am Ceram Soc 96:1673–1681
25. Khomskii D (2009) Classifying multiferroics: Mechanisms and effects. Physics 2: doi:10.1103/Physics.2.20
26. Kinoshita K, Yamaji A (1976) Grain-size effects on dielectric properties in barium titanate ceramics. J Appl Phys 47:371–373
27. Lee JS, Boyd JG, Lagoudas DC (2005) Effective properties of three-phase electro-magneto-elastic composites. Int J EngSci 43(10):790–825
28. Martin L, Chu YH, Ramesh R (2010) Advances in the growth and characterization of magnetic, ferroelectric, and multiferroic oxide thin films. Mater Sci Eng 68(46):89–133. doi:10.1016/j.mser.2010.03.001
29. Nan CW (1994) Magnetoelectric effect in composites of piezoelectric and piezomagnetic phases. Phys Rev B 50:6082–6088. doi:10.1103/PhysRevB.50.6082
30. Nan CW, Liu G, Lin Y, Chen H (2005), Magnetic-field-induced electric polarization in multiferroic nanostructures. Phys Rev Lett 94(19):197,203-1-4
31. Nan CW, Bichurin MI, Dong S, Viehland D, Srinivasan G (2008) Multiferroic magnetoelectric composites: historical perspective, status, and future directions. J Appl Phys 103(3):031101
32. Priya S, Islam R, Dong S, Viehland D (2007) Recent advancements in magnetoelectric particulate and laminate composites. J Electroceram 19(1):147–164
33. Ramesh R, Spaldin N (2007) Multiferroics: progress and prospects in thin films. Nat Mater 6(1):21–29
34. Rauscher M, Roosen A (2009) Effect of particle shape on anisotropic packing and shrinkage behavior of tape-cast glass-ceramic composites. Int J Appl Ceram Technol 6:24–34
35. Ryu J, Priya S, Uchino K, Kim HE (2002) Magnetoelectric effect in composites of magnetostrictive and piezoelectric materials. J Electroceram 8(2):107–119
36. Schmid H (1994) Multi-ferroic magnetoelectrics. Ferroelectrics 162:317–338
37. Schröder J (2009) Derivation of the localization and homogenization conditions for electro-mechanically coupled problems. Comput Mater Sci 46(3):595–599
38. Schröder J, Gross D (2004) Invariant formulation of the electromechanical enthalpy function of transversely isotropic piezoelectric materials. Arch Appl Mech 73:533–552
39. Schröder J, Keip MA (2012) Two-scale homogenization of electromechanically coupled boundary value problems. Comput Mech 50:229–244
40. Schröder J, Keip MA, Labusch M (2014) Algorithmic two-scale transition for magneto-electro-mechanically coupled problems—localization and homogenization (in preparation)
41. Srinivas S, Li JY (2005) The effective magnetoelectric coefficients of polycrystalline multiferroic composites. Acta Mech 53(15):4135–4142
42. Srinivas S, Li JY, Zhou YC, Soh AK (2006) The effective magnetoelectroelastic moduli of matrix-based multiferroic composites. J Appl Phys 99(4):043,905
43. Srinivasan G (2010) Magnetoelectric composites. Annu Rev Mater Res 40:1–26

44. van Suchtelen J (1972) Product properties: a new application of composite materials. Philips Res Rep 27:28–37
45. Wang T, Wang X, Yao G, Zhang Y, Liao X, Yang G, Song TH, Li L (2008) Effects of processing on microstructure and dielectric properties of ultrafine-grained barium titanate based ceramics for bme-mlcc applications. Key Eng Mater 368–372:43–46
46. Wang Y, Hu J, Lin Y, Nan CW (2010) Multiferroic magnetoelectric composite nanostructures. Nat Asia-Pac Asia Mater 2:61–68
47. Waser R, Baiatu T, Härdtl KH (1990) dc electrical degradation of perovskite-type titanates. J Am Ceram Soc 73:1645–1653
48. Zohdi T (2010) Simulation of coupled microscale multiphysical-fields in particulate-doped dielectrics with staggered adaptive fdtd. Comput Methods Appl Mech Eng 199:3250–3269
49. Zohdi T (2012) Electromagnetic properties of multiphase dielectrics. Springer, Berlin